

2D particle-in-cell simulations of geometrically asymmetric low-pressure capacitive RF plasmas driven by tailored voltage waveforms

Li Wang^{1,2}, Peter Hartmann³, Zoltán Donkó³, Yuan-Hong Song^{1,*}
and Julian Schulze^{1,2}

¹ Key Laboratory of Materials Modification by Laser, Ion, and Electron Beams (Ministry of Education), School of Physics, Dalian University of Technology, Dalian 116024, People's Republic of China

² Department of Electrical Engineering and Information Science, Ruhr-University Bochum, D-44780, Bochum, Germany

³ Institute for Solid State Physics and Optics, Wigner Research Centre for Physics, H-1121 Budapest, Konkoly-Thege Miklós str. 29-33, Hungary

E-mail: songyh@dlut.edu.cn

Received 8 December 2020, revised 25 February 2021

Accepted for publication 29 March 2021

Published 19 May 2021



CrossMark

Abstract

The effects of the simultaneous presence of two different types of plasma asymmetry, viz, geometric and electrical, on low-pressure capacitively coupled argon discharges are studied by 2D3V graphics-processing-unit-based particle-in-cell/Monte Carlo simulations. The geometric asymmetry originates from the different powered vs grounded electrode surface areas, while the electrical asymmetry is established by applying peaks/valleys and sawtooth-up/-down driving voltage waveforms. While in geometrically symmetric discharges, the {peaks ↔ valleys} and the {sawtooth-down ↔ sawtooth-up} switching of the waveforms is equivalent to exchanging the powered and grounded electrodes, this transformation is violated when the geometric symmetry is broken. Under such conditions, the plasma characteristics and the DC self-bias generation behave differently, compared to the geometrically symmetric case. This leads to different sheath dynamics and, therefore, strongly influences the electron power absorption dynamics. For identical peak-to-peak voltages, the plasma density obtained for such tailored voltage waveforms is found to be higher compared to the classical single-frequency waveform case. Reduced plasma densities are found in the valleys- and sawtooth-down waveform cases, compared to the peaks- and sawtooth-up waveforms. By including realistic energy and material-dependent secondary electron emission (SEE) coefficients in the simulations, the electron-induced SEE is found to be reduced in the valleys- and sawtooth-down waveform cases, which explains the behaviour of the plasma density. Using such tailored waveforms in geometrically asymmetric discharges is also found to lead to the formation of different charged particle energy distributions at the boundary surfaces, compared to those in geometrically symmetric plasma sources.

Keywords: capacitively coupled plasmas, geometrically asymmetric capacitively coupled plasmas, 2D simulations, voltage waveform tailoring, realistic plasma-surface interactions

(Some figures may appear in colour only in the online journal)

*Author to whom any correspondence should be addressed.

1. Introduction

Capacitively coupled plasmas (CCPs) are one of the most important systems used in different plasma-processing applications such as etching, deposition, and sputtering [1–4]. Particular applications usually require different plasma properties, e.g., etching usually needs high-energy ion bombardment of the wafer at energies of up to hundreds or thousands of eV [5, 6]; deposition demands low ion energies of several tens of eV or less, to prevent damage to surface films. High ion fluxes are required for both processes to ensure high process rates. Therefore, good control of the particle flux, energy, and incident angle at the surface is important for CCP applications [7–10].

The electrical asymmetry effect (EAE), which was first proposed by Heil *et al* in 2008 [11–14], provides a good way to improve the independent control of ion properties, i.e. ion flux and energy, at boundary surfaces. The authors demonstrated that by driving the discharge with a fundamental frequency and its second harmonic, a DC self-bias is generated, which electrically induces a plasma asymmetry in geometrically symmetric reactors. The DC self-bias can be tuned by adjusting the phase angle between the two harmonics, which allows control of ion energies at the boundary surfaces while keeping the ion flux almost constant. In the following studies of controlling plasma parameters via voltage waveform tailoring (VWT), additional waveform shapes were proposed that used a higher number of harmonics. Depending on the shape of the driving voltage waveform, two different types of electrical asymmetry were discovered, i.e. the amplitude asymmetry effect (AAE) and the slope asymmetry effect (SAE) [15–20]. The AAE is induced by voltage waveforms with different positive and negative extrema, such as peaks- and valleys-waveforms. The SAE is induced by using temporally asymmetric waveforms characterized by different rising and falling slopes, such as sawtooth-up and sawtooth-down waveforms. In addition to enhanced control of ion properties, the use of such waveforms was also found to allow control of the electron power absorption dynamics and the electron energy distribution function by customizing the spatio-temporal distribution of the electric field in the plasma [21–28] and was found to optimize plasma uniformity [29–34]. Overall, the control of particle properties via these tailored voltage waveforms (TVWs) has received considerable interest in recent years. Thus, this topic has been investigated both numerically and experimentally and has even been used for applications [35–43]. VWT has been demonstrated to be a robust technique. In fact, any existing CCP can be extended to use VWT by modifying the external circuits of existing reactors, i.e., the existing RF generators and impedance matching [44–46]. The reactor itself does not need any modification.

Despite the intensive investigations of TVWs in CCPs, which provided valuable insights into the discharge properties and various concepts for the control of plasma characteristics, most of the simulations have been conducted for geometrically symmetric systems. However in reality, most

CCP reactors are geometrically asymmetric [47–51]. The surface area of the grounded electrode in such systems is larger than that of the powered electrode, which leads to the generation of a negative DC self-bias and the formation of a high-voltage sheath at the powered electrode. This, in turn, leads to different sheath dynamics at the powered and grounded electrodes, and thus to asymmetric charged particle dynamics at both electrodes, i.e., to different electron and ion power absorptions near the two electrodes. This geometric asymmetry is known to greatly influence the plasma density and charged particle distribution functions at the surfaces, which further affect the etching or deposition quality and efficiency [52, 53].

Several previous simulation and experimental studies have pointed out a coupling of the electrical and geometric asymmetry effects [26, 54–57]. It has been demonstrated that by tuning the phase shift between two consecutive driving harmonics, the asymmetry generated by the reactor geometry can be enhanced or suppressed by the electrical asymmetry. While these studies revealed important insights into the consequences of the EAE on geometrically asymmetric and commercially relevant CCPs, they left a number of important questions open: how does the use of different types of TVW (synthesized from more than two harmonics) affect the sheath dynamics at both electrodes in geometrically asymmetric CCPs? How does this affect the electron power absorption dynamics and the formation of the charged particle distribution functions? And how is all this affected by material- and energy-dependent plasma-surface interactions such as secondary electron emission (SEE)? Answering these research questions is highly relevant to both fundamental and applied research, since, in fact, VWT may lead to completely different effects in geometrically asymmetric compared to geometrically symmetric reactors. In particular, for discharges operated at low pressure, which are frequently used for plasma etching and sputtering, the plasma-surface interactions can significantly influence the discharge [58–61]. In these cases, the secondary electron yields and the complex heating dynamics of different electron groups are sensitive to the changes of the sheath dynamics and can strongly affect the ionization and the plasma density.

Computational investigations of application-relevant reactor geometries and low-pressure plasmas require the use of kinetic 2D3V particle-in-cell simulations complemented by a Monte Carlo treatment of collisions (PIC/MCC). To ensure accurate simulation results, SEE induced by different particle species at boundary surfaces must be realistically included [58, 62]. In earlier studies of ion-induced secondary electron (γ -electron) emission, a constant emission coefficient was usually set in the simulations due to a lack of data for the energy- and material-dependent surface coefficients. Despite this, such studies reported strong effects of the γ -electron emission coefficients (the γ -coefficient) on the discharge operation mode [63–68]. When a low γ -coefficient was used in the simulations of argon discharges, the discharge was usually found

to operate in the α -mode [69]. When the γ -coefficient was increased, the γ -mode was found to dominate the discharge [70, 71]. Such mode transitions were also observed when the gas pressure and the driving voltage amplitude increased. In multi-frequency discharges, the γ -coefficient was found to affect the ion flux and energy distribution functions at boundary surfaces [72, 73]. Lafleur *et al* and Korolov *et al* demonstrated that different γ -coefficients at the two electrodes (representing different electrode materials) can lead to a (surface-induced) plasma asymmetry [74, 75]. In recent years, plasma-surface interaction processes have been taken into account more precisely in simulations [58]. For instance, energy- and material-dependent γ -electron emission models have been implemented in some PIC/MCC simulations [76]. By comparing the results from such models with the results obtained by assuming constant γ -coefficients in the simulations, Daksha *et al* [77–79] pointed out that neglecting the energy-dependence of γ -coefficients may lead to unrealistic results in many cases. They also demonstrated the effects of the surface material and surface properties on the discharge operation mode and the charged particle distributions at boundary surfaces. Moreover, the effects of realistic electron-surface interactions on low-pressure CCP discharges have recently been studied by Horváth *et al* [80–82]. In the simulations, they took into account elastic electron reflection, inelastic backscattering, and electron-induced secondary electron (δ -electron) emission. The surface coefficients of such processes are considered to depend on the surface material as well as on the energy and angle of incidence of the electrons reaching the surface. The electron power absorption and ionization dynamics were found to be very different from the results obtained from a simplified electron-surface interaction model. In the more realistic case, γ -electrons generated at one electrode and accelerated towards the plasma bulk were found to bombard the opposite electrode at very high energies and to induce a large number of δ -electron emissions at this electrode. The emitted δ -electrons were able to contribute to the ionization, excitation, and dissociation of the background gas. In the most recent studies, both realistic ion-induced and electron-induced SEE processes have been implemented in 1D PIC/MCC simulations [83, 84]. However, the effects of such a realistic treatment of plasma-surface interactions in geometrically asymmetric CCPs driven by TVWs have not been studied yet. Such studies of application-relevant reactor geometries require 2D PIC/MCC simulations.

In this work, we study geometrically asymmetric CCPs driven by TVWs and operated in argon gas at low pressure using graphics-processing-unit(GPU)-based 2D electrostatic PIC/MCC simulations including realistic ion- and electron-induced SEE coefficients. We reveal the unique effects of different types of TVWs (peaks, valleys, sawtooth-up, and -down) on the electron power absorption dynamics, on the formation of charged particle distribution functions, and on the emission of secondary electrons as well as their role in the plasma. These findings differ strongly from the effects of such TVWs on the plasmas in geometrically symmetric CCPs studied previously. These differences are explained by the constructive/destructive ‘interference’ of different types of

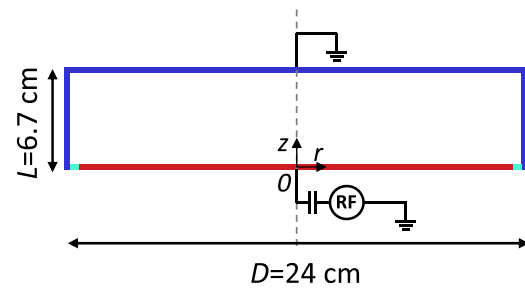


Figure 1. The reactor geometry investigated. The powered and grounded electrodes are indicated by the red and blue lines, respectively. The areal ratio between the powered and grounded electrodes is $A_P/A_G = 0.46$.

electrical asymmetry induced by the respective driving voltage waveforms, the geometric reactor asymmetry, and a detailed analysis of its consequences on the electron power absorption dynamics. Since most commercial CCPs are geometrically asymmetric and our findings differ significantly from those of previous studies obtained in (idealized) 1D geometrically symmetric settings, these findings are expected to be highly relevant to fundamental and applied research in low-temperature plasma science.

This paper is structured in the following way: the 2D PIC/MCC simulation, including the realistic SEE model, is described in section 2. In section 3, we describe our study of the effects of two different types of electrical asymmetry induced by different TVWs (peaks-/valleys- and sawtooth waveforms) on the discharge. First, the basic plasma characteristics such as the electron density and the DC self-bias are compared for different driving voltage waveform shapes with identical peak-to-peak voltages (section 3.1). The effects of the amplitude asymmetry induced by peaks- and valleys-waveforms (section 3.2) and of the slope asymmetry induced by sawtooth waveforms (section 3.3) on the geometrically asymmetric CCP are then analysed in detail. Finally, concluding remarks are given in section 4.

2. Simulation method

In this work, we simulate plasmas in argon gas using a cylindrical 2D3V (two-dimensional in space and three-dimensional in velocity space) electrostatic particle-in-cell/Monte Carlo collision code. The radial and axial directions are resolved in the simulations and azimuthal symmetry is assumed. The plasma is operated in a geometrically asymmetric reactor, as shown in figure 1. The ratio between the areas of the powered electrode (red line) and the grounded electrode (blue line) is 0.46. The diameter of the reactor is 24 cm and the gap between the plane parallel sections of both electrodes is 6.7 cm. A dielectric spacer (light green line) with a length of 2.5 mm is inserted between the two electrodes in the simulations, across which the potential is assumed to drop linearly. Although more complicated geometries [85, 86] including side flanges and gas/plasma volumes in between the radial electrode edges and the side walls are sometimes used in commercial CCP reactors, the simplified geometry shown in figure 1 provides important general insights into the plasma

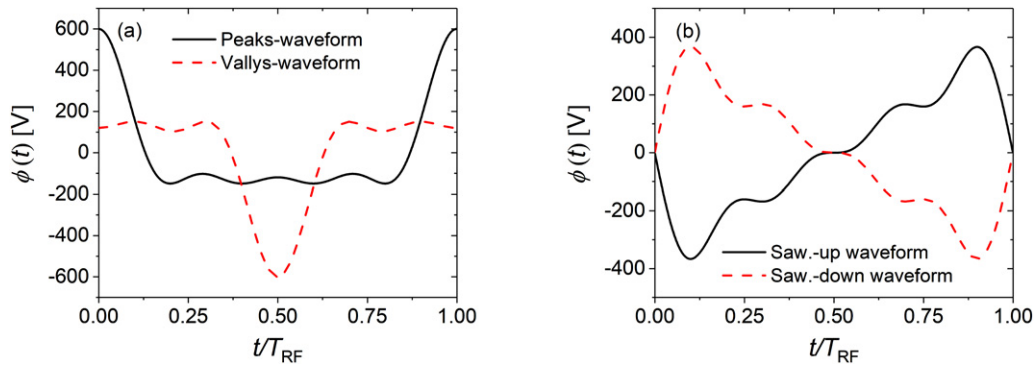


Figure 2. Driving voltage waveforms used in the simulations. (a) Peaks- and valleys-type waveforms (with $N = 4$ harmonics); and (b) sawtooth waveforms ($N = 4$). T_{RF} is the period of the fundamental frequency, $f = 13.56$ MHz. The peak-to-peak voltage is $\phi_{\text{pp}} = 750$ V in all cases.

characteristics in geometrically asymmetric experimental systems. Moreover, reactor geometries such as those investigated in this work are, in fact, used for both experiments and applications [52, 53, 87].

Our simulation code traces electrons and Ar^+ ions. The elementary processes include elastic scattering, excitation into 25 individual levels, and ionization in e^- -Ar atom collisions; elastic scattering (including an isotropic and a backward (charge exchange) scattering channel), excitation into three individual levels, and ionization in Ar^+ -Ar collisions. Under the discharge conditions studied in this work, ionization caused by metastable pooling, stepwise ionization, and the contribution of metastable atoms to the generation of secondary electrons at the electrodes are expected to be unimportant. Therefore, these effects are neglected in the simulations [76, 88, 89]. The cross-sections and more detailed information concerning the handling of collision processes in our code can be found in references [83, 90–98].

Several different driving voltage waveforms are used in this work.

- The effects of an electrically induced amplitude asymmetry on the discharge are studied by using peaks- and valleys-waveforms according to:

$$\phi(t) = \sum_{k=1}^N \phi_k \cos(2\pi k f t + \theta_k), \quad (1)$$

where N is the number of consecutive harmonics, and θ_k are the harmonics' phase angles. Here, we study the case $N = 4$ with a fundamental frequency of $f = 13.56$ MHz. By setting all θ_k to zero, peaks-type waveforms can be realized, while valleys-type waveforms are realized by setting the phase angles of the even harmonics to π . The amplitude ϕ_k of each harmonic is:

$$\phi_k = \frac{2(N - k + 1)}{(N + 1)^2} V_{\text{pp}}, \quad (2)$$

where ϕ_{pp} is the peak-to-peak voltage, which is set to 750 V in this work. The peaks- and valleys-waveforms applied in this work are shown in figure 2(a).

- The effects of an electrically induced slope asymmetry on the discharge are studied by using sawtooth waveforms:

$$\phi(t) = \pm \phi_{\text{pp}} \sum_{k=1}^N \frac{1}{k} \sin(2\pi k f t). \quad (3)$$

Sawtooth-up and -down type waveforms can be realized by setting the sign to minus and plus, respectively. The sawtooth waveforms applied in this work are shown in figure 2(b), for $N = 4$, $f = 13.56$ MHz, and $\phi_{\text{pp}} = 750$ V.

A realistic model is used in the simulations to describe the interactions of the plasma species with SiO_2 boundary surfaces, which was introduced in detail in our previous works [83, 99]. The energy-dependent Ar^+ -ion-induced SEE coefficient is adopted from the work of Phelps and Petrović [100] to describe the SE yield at the oxidized metal surface. Similar ion-induced SE yields of SiO_2 surfaces were found experimentally by Sobolewski [101]. For the electron surface interactions, we include three processes, i.e. elastic electron reflection, inelastic electron reflection, and electron-induced SEE. The coefficients of these processes depend on the incident energy and angle as well as the surface material. We adopt these coefficients for electron interactions with SiO_2 from the work of Horvath *et al* [80, 81, 83].

In this work, the gas temperature is fixed at 400 K and the neutral gas pressure is 0.5 Pa. Such discharge conditions are representative of the non-local regime in CCPs, where the electron mean free path is longer than the electrode gap, so that energetic electrons generated at one electrode can reach the opposite electrode collisionlessly. Studying this regime is of high fundamental relevance, since the basics of non-local and non-linear electron dynamics and plasma-surface interactions are not entirely understood. Moreover, such conditions are important for a variety of applications of CCPs, such as plasma etching and sputtering. Under the conditions considered ($f = 13.56$ MHz, $V_{\text{pp}} = 750$ V, and a 24 cm electrode diameter), to a good approximation, electromagnetic effects can be ignored. In our 2D simulations, 512 to 1024 grid points in the radial and axial directions, respectively, are used for different simulation cases to resolve the Debye-length. Particles are traced using at least 8000 timesteps per RF period, to provide suffi-

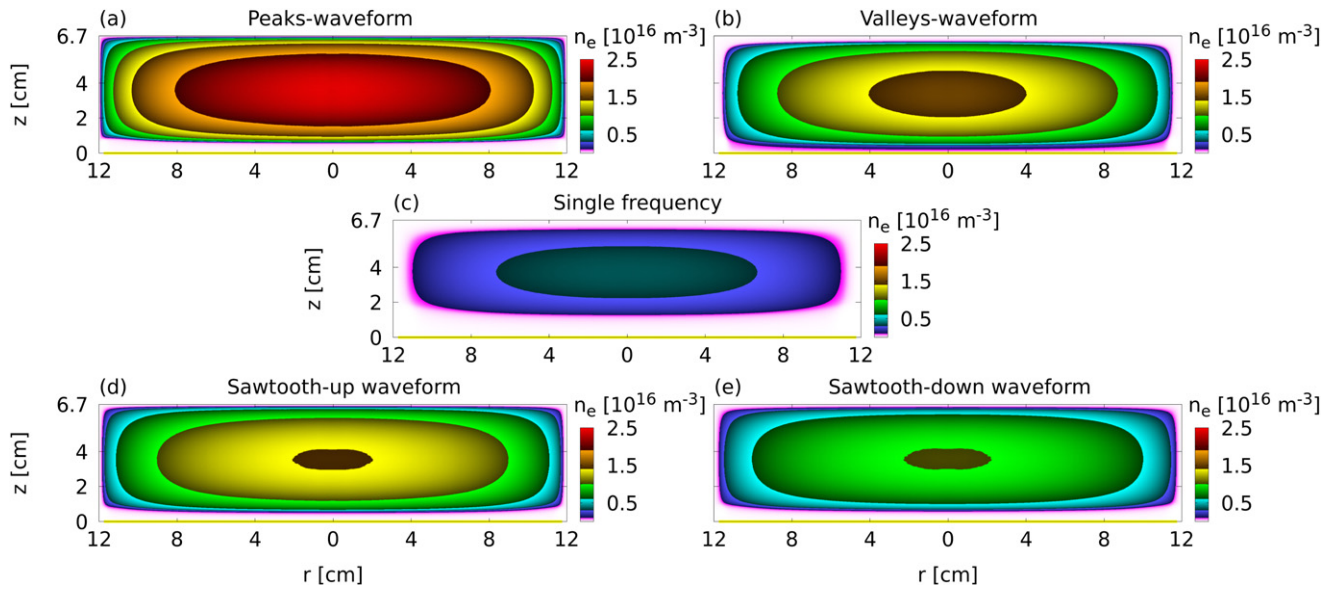


Figure 3. 2D spatial distributions of the time-averaged electron density for peaks- (a) and valleys- (b) waveforms, the single-frequency case (c), and sawtooth-up (d), sawtooth-down (e) waveforms. Discharge conditions: Ar, $V_{pp} = 750$ V, $f = 13.56$ MHz, and $N = 4$ (except for the single-frequency case), electrode gap $L = 6.7$ cm, electrode radius $r = 12$ cm, gas pressure $p = 0.5$ Pa, gas temperature $T = 400$ K, and SiO_2 surfaces.

cient accuracy for computing their trajectories and to fulfil all stability criteria. The number of superparticles ranges between 10^7 and 5×10^7 . This represents a high computational demand and, therefore, we use a GPU and the Nvidia Compute Unified Device Architecture programming language to perform the simulations. Each particle is assigned to an individual computational thread and all PIC/MCC steps and diagnostic routines are executed in parallel on the GPU. The Poisson equation is solved iteratively using the ‘red/black’ parallel version of the successive over-relaxation method [102, 103]. The time evolution of the super-particle number is examined for each charged particle species while running each simulation case. Convergence is achieved when the particle number becomes constant (except for some statistical fluctuations) for each of the species. It takes around one week to reach convergence for each case, which is about 100 times faster than sequential CPU simulations.

3. Results

3.1. Comparison of the basic plasma behaviours for different driving voltage waveforms

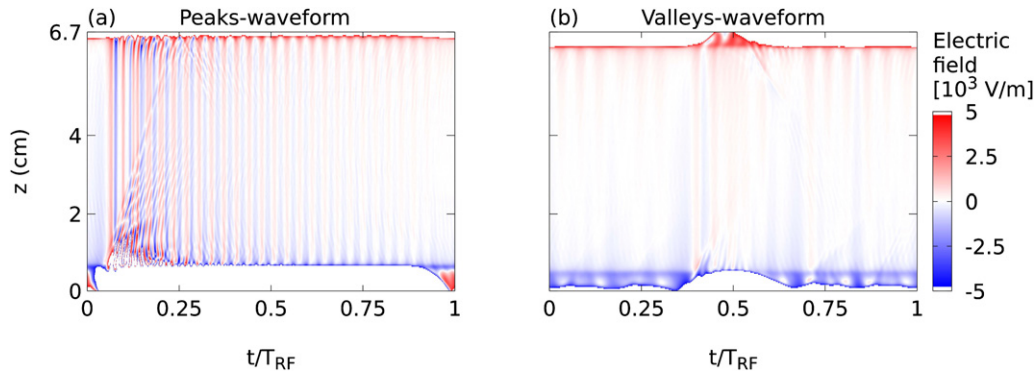
First, we compare the basic plasma behaviour in the geometrically asymmetric reactor at 0.5 Pa in argon gas for different driving voltage waveforms with identical peak-to-peak voltage amplitudes of 750 V. Figure 3 shows the 2D spatial distributions of the time-averaged electron density for a single frequency along with peaks-, valleys-, sawtooth-up and sawtooth-down waveforms. The peak electron density and the DC self-bias voltage for these cases are listed in table 1. Due to the presence of higher-frequency components and kinetic effects that will be discussed in more detail in the following sections, the electron densities in the VWT cases are

significantly higher than the density in the single-frequency case. The peak electron density ratios are 1:6.9:4.3:4.0:2.9 for the single-frequency, peaks-, valleys-, sawtooth-up, and -down waveform cases. As opposed to geometrically symmetric reactors, where switching the driving voltage waveform from the peaks- to valleys-type results in the same plasma density and ion flux at a given electrode [9, 21, 104], here, a difference of a factor of 1.6 in the plasma density is found between these two cases. This is caused by the ‘superposition’ of the geometric asymmetry and the electrical asymmetry, which can be either constructive (peaks-waveform, high plasma density) or destructive (valleys-waveform, low plasma density). The DC self-bias caused by the geometric asymmetry in the single-frequency case is -220 V in the absence of any electrical asymmetry. The peaks-waveform enhances the asymmetry of the discharge, which leads to the generation of a more negative DC self-bias of -512 V. The plasma density maximum shifts towards the top (grounded) electrode. In the valleys-waveform case, however, the geometric asymmetry is compensated for by the electrical asymmetry, which leads to a positive DC self-bias of 60 V. These results are in agreement with the experimental findings of Berger *et al* [26] and Schuengel *et al* [56], where these constructive and destructive superposition effects of the geometric and electrical asymmetry on the DC self-bias were observed as well.

Compared to the sawtooth-up waveform case, the electron density is found to be reduced by a factor of 0.72 in the sawtooth-down waveform case. Under the low-pressure conditions studied here, the sawtooth-up and -down waveforms do not lead to significantly different values of the DC self bias (-237 V and -215 V, respectively). Comparing the electron densities obtained for sawtooth waveforms with those characterising the peaks- and valleys-waveforms, the peaks-waveform is found to result in the highest plasma density under

Table 1. Peak electron densities and DC self-bias voltages for the cases studied.

Waveform shape	DC self-bias	Peak electron density
Single frequency	−220 V	$0.35 \times 10^{16} \text{ m}^{-3}$
Peaks	−512 V	$2.44 \times 10^{16} \text{ m}^{-3}$
Valleys	60 V	$1.52 \times 10^{16} \text{ m}^{-3}$
Sawtooth-up	−237 V	$1.42 \times 10^{16} \text{ m}^{-3}$
Sawtooth-down	−215 V	$1.02 \times 10^{16} \text{ m}^{-3}$

**Figure 4.** Axially and temporally resolved electric fields for peaks- (a) and valleys- (b) waveforms. The results are obtained by averaging the data in the radial direction within the central region of the reactor ($r \leq 6$ cm). The discharge conditions are the same as in figure 3.

otherwise identical discharge conditions. This is mainly caused by the different sheath and electron power absorption dynamics induced by the different driving voltage waveforms, which will be explained in detail in the following. We only observe a small axial asymmetry of the density profiles, which is specific to each driving voltage waveform shape due to the different sheath widths at the powered and grounded electrodes. The various waveforms do not lead to significant asymmetry because of the non-local conditions under the low gas pressure studied here, i.e. the electron mean free path is so long that electrons can ionize the neutrals in the whole bulk region after being accelerated by the expanding sheath. By comparing the ratio of the ion flux to the powered electrode near the radial centre to the ion flux near the sidewall for the different simulation cases (not shown here), the effect of different types of driving voltage waveform on the radial plasma uniformity is found to be negligible under the discharge conditions studied here.

3.2. Detailed analysis of the peaks- and valleys-waveform cases

In this section, we study the effects of an electrically induced amplitude asymmetry in geometrically asymmetric discharges in detail using peaks- and valleys-waveforms. Figure 4 shows the axially and temporally resolved electric fields for these two cases. The superposition of the geometric asymmetry and the electrical amplitude asymmetry caused by the peaks- and valleys-waveforms results in very different sheath dynamics. In the peaks-waveform case, a large sheath is formed at the powered electrode due to the strong negative DC self-bias as

a result of the constructive superposition of both asymmetries. During the sheath expansion phase at the powered electrode, the fast sheath expansion leads to the excitation of strong plasma series resonance (PSR) oscillations [105–110]. During the sheath collapse phase at the powered electrode, an electric field reversal is generated, for two reasons: first, the electrons cannot follow the fast sheath collapse by diffusion, due to their inertia. Second, the large sheath voltage drop at the powered electrode enhances the ion bombardment energy, and thus, the γ -electron emission, which effectively reduces the electron flux towards the electrode. In order to compensate for the ion flux to this electrode on time average, a field reversal is generated to accelerate electrons towards this electrode. In this case, a narrow sheath is formed at the grounded electrode. In the valleys-waveform case, the sheath is expanded for a long time and only collapses once within each fundamental RF cycle at the grounded electrode. Due to the destructive superposition of the electrical amplitude asymmetry and the geometric asymmetry, the DC self-bias is low and positive (60 V). Consequently, the maximum sheath width at the grounded electrode is smaller, compared to the maximum sheath width at the powered electrode in the presence of the peaks-waveform. Therefore, the PSR is excited less strongly and the electric field reversal during sheath collapse is much less pronounced in the valleys- compared to the peaks-waveform case.

The axially and temporally resolved total ionization rates as well as the ionization rates of different electron groups (bulk, γ -, and δ -electrons) are shown in figure 5 for the peaks- and valleys-waveform cases. In the peaks-waveform case, several fast electron beams are generated during the sheath expansion at the powered electrode. This is caused by the self-excitation

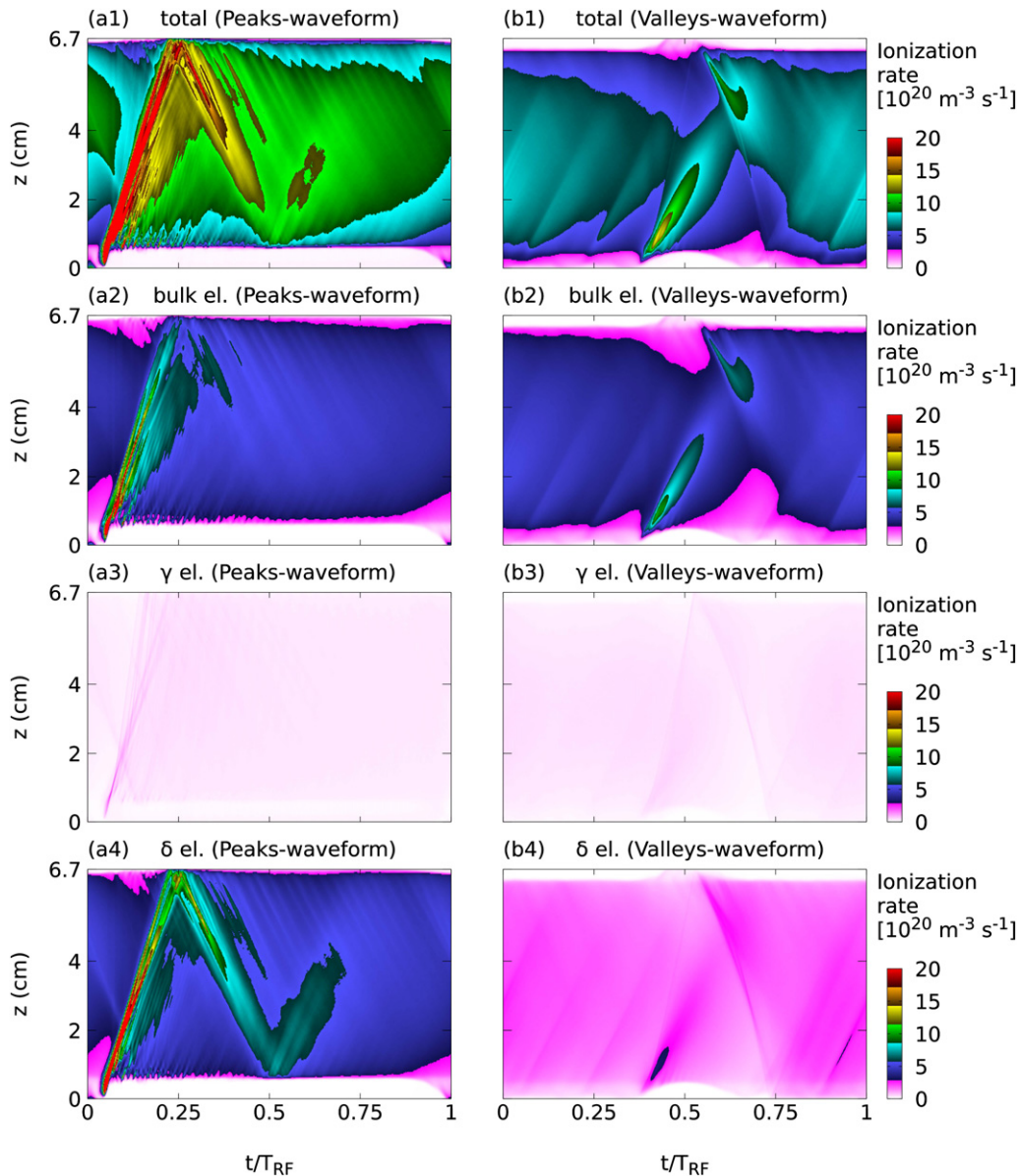


Figure 5. Axially and temporally resolved plots of the total ionization rate (first row), the ionization rate of bulk electrons (second row), γ -electrons (third row), and δ -electrons (fourth row) for the peaks- and valleys-waveforms. These results are obtained by averaging the data in the radial direction within the central region of the chamber ($r < 6$ cm). The discharge conditions are the same as in figure 3.

of the PSR [108, 111]. The beam electrons accelerated by the fast expanding sheath cause strong ionization. Moreover, some of these electrons penetrate through the plasma bulk and bombard the grounded electrode during the local sheath collapse. Therefore, a high number of δ -electrons is emitted at the grounded electrode, which causes additional ionization, as shown in figure 5(a4). The δ -electrons contribute around 52% of the total ionization in this case. Due to the fast sheath expansion at the powered electrode, γ -electrons emitted from this electrode during the local sheath collapse are accelerated by the sheath expansion, and also cause ionization (see figure 5(a3)). During the long period of full sheath expansion at the powered electrode, γ -electrons emitted by this boundary are accelerated by the strong sheath electric field

towards the bulk. These γ -electrons are too energetic to ionize the neutrals.

In the valleys-waveform case, the sheath expansion at the powered electrode is slower and, thus, the electron power absorption by sheath expansion heating is weaker. Therefore, a smaller ionization rate is found in figure 5(b1) compared to figure 5(a1), which is one important reason for the decreased plasma density. After being accelerated by the expanding sheath at the powered electrode, electrons propagate through the bulk region, and arrive at the grounded electrode. In contrast to the peaks-waveform case, these electrons arrive at the opposite electrode at a time when the local sheath is expanded. Thus, most of them are reflected by the sheath and have no chance of hitting the grounded electrode and of emitting δ -

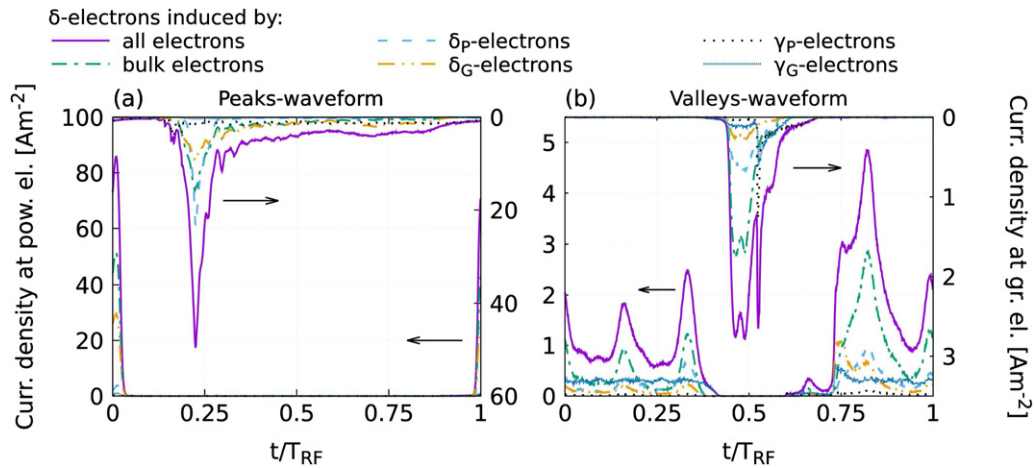


Figure 6. Time-dependent current density of emitted δ -electrons induced by different electron groups at the planar part of the grounded electrode (top and right axes) and at the powered electrode (bottom and left axes). The discharge conditions are the same as in figure 3.

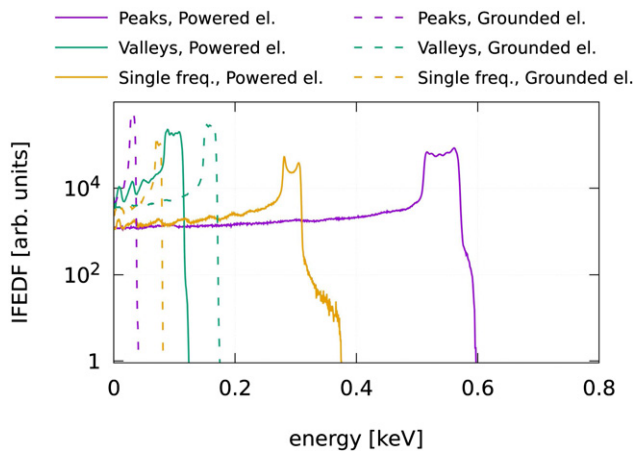


Figure 7. Radially averaged IFEDF at the powered electrode and at the planar part of the grounded electrode for peaks- and valleys-waveforms and for the single-frequency case. The discharge conditions are the same as in figure 3.

electrons. Consequently, the δ -electrons cause only 29% of the total ionization in this scenario, which is much less than the peaks-waveform case, as shown in figures 5(b4) and (a4). This is the second reason for the decreased plasma density in the valleys-waveform case. Similar coupling effects of electrical amplitude asymmetries caused by peaks- and valleys-waveforms with geometric reactor asymmetries on spatio-temporal electron dynamics were experimentally observed by Berger *et al* [26].

Figure 6 shows the time-dependent current density of δ -electrons emitted at the electrodes induced by different electron groups. Since the generation of δ -electrons due to electrons created in $\text{Ar}^+ + \text{Ar}$ ionizing collisions is negligible, it is not shown in this figure. In the peaks-waveform case, the fast sheath expansion at the powered electrode gives rise to high energy bulk and δ -electron beams. These beams propagate through the bulk region and bombard the grounded electrode with high energies, which leads to a large number of δ -electron emissions at the time around $t/T_{\text{RF}} = 0.23$, as shown in figure 6(a). At the powered electrode, due to the

large sheath potential, δ -electrons are only emitted over a very short time period when the local sheath collapses. Most of these δ -electrons are emitted by bulk electrons and δ -electrons emitted at the grounded electrode. Compared to the peaks-waveform case, much less δ -electrons are emitted in the valleys-waveform case, as shown in figure 6(b). At the grounded electrode, most of the δ -electrons are emitted during the local sheath collapse at the time around $t/T_{\text{RF}} = 0.5$. Besides the peak caused by bulk electrons, another sharp δ -electron emission peak is observed, which is mainly induced by γ - and δ -electrons emitted at the powered electrode inside the local high-voltage sheath, where they are accelerated towards the plasma bulk by the local sheath electric field and finally bombard the grounded electrode at high energies. At the powered electrode, several δ -electron emission peaks are observed, which correspond to the multiple sheath collapses at this electrode within each fundamental RF period. Compared to the first half of the RF period, the peak value of the δ -electron emission at the powered electrode is stronger in the second half of the fundamental RF period. This is because the sheath expansion at the grounded electrode pushes electrons towards the powered electrode at the beginning of the second half of the fundamental RF period, which increases the electron bombardment energy at the powered electrode during this time window and finally leads to more δ -electron emissions. Moreover, due to the large sheath at the grounded electrode, the γ -electrons emitted at the grounded electrode can be accelerated to high energies over a long period of time. Therefore, they can induce δ -electron emission at the powered electrode during a long fraction of the fundamental RF period.

Figure 7 shows the ion flux-energy distribution functions at the electrodes for peaks- and valleys-waveforms and for the single-frequency case. By changing the driving voltage waveform, the ion flux-energy distribution functions (IFEDFs) at the electrodes can be modified significantly. In the peaks-waveform case, the ions bombard the powered electrode with energies of up to 600 eV due to the high negative DC self-bias caused by the constructive superposition of the

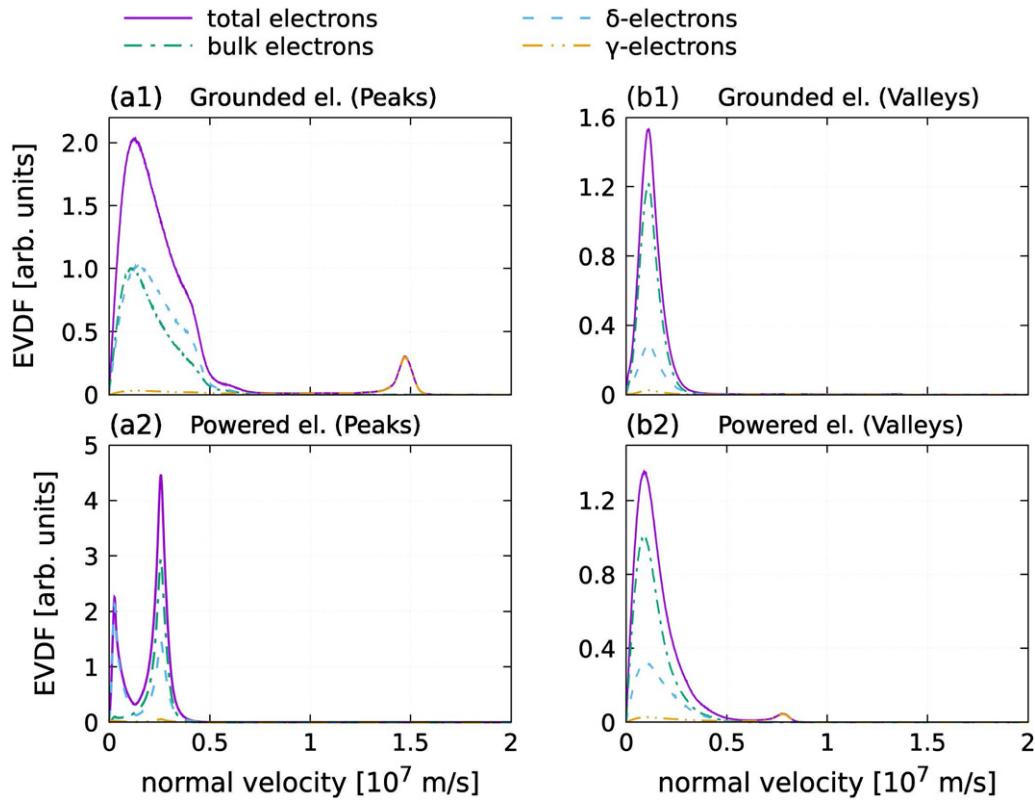


Figure 8. EVDF at the powered electrode and at the planar part of the grounded electrode for peaks- (first column) and valleys-waveforms (second column). The discharge conditions are the same as in figure 3.

electrical amplitude and the geometric asymmetry of the discharge. Due to the low-voltage sheath at the grounded electrode, the ion bombardment energy at this electrode is less than 50 eV. In the valleys-waveform case, the difference of the ion bombardment energies at the powered and grounded electrodes is small due to the low DC self-bias caused by the destructive superposition of the electrical amplitude and the geometric discharge asymmetry. The highest ion bombardment energy at the powered electrode is about 120 eV, which is much lower than that found in the peaks-waveform case. Similar coupling effects of electrical amplitude asymmetries caused by peaks- and valleys-waveforms with geometrical reactor asymmetries on the IFEDF at the electrodes were experimentally observed by Berger *et al* [26]. In the single-frequency case, the highest ion bombardment energy is around 370 eV at the powered electrode, which is smaller compared to the peaks-waveform case, but higher than the valleys-waveform case due to the DC self-bias caused by the geometric asymmetry.

The electron velocity distribution functions at the electrodes are shown in figure 8. Since the number of electrons generated by ion-induced ionization that arrives at the electrodes is negligible, it is not shown in this figure. In the peaks-waveform case, γ -electrons emitted at the powered electrode can be accelerated to high energies by the strong local sheath electric field and bombard the grounded electrode at high velocities, as shown in figure 8(a1). At the powered

electrode, such highly energetic γ -electrons are absent, due to the low sheath voltage at the grounded electrode and the short sheath collapse at the powered electrode. Nevertheless, a large peak appears at a relatively high velocity in figure 8(a2). This is because the bulk and δ -electrons originating from the bulk region are accelerated by the strong local electric field reversal during the local sheath collapse upon their approach to the electrode. Moreover, a number of δ -electrons is found to bombard the powered electrode at low energies, which form a peak at low velocities in figure 8(a2). These are δ -electrons newly emitted by the adjacent electrode which have low initial energies and are immediately dragged back to the powered electrode by the reversed field. In contrast to the peaks-waveform case, a relatively large high-voltage sheath is generated at the grounded electrode in the valleys-waveform case. Thus, γ -electrons emitted at the grounded electrode can be accelerated to high energies in the local sheath and bombard the powered electrode at high velocities, as shown in figure 8(b2). Therefore, switching from the peaks- to the valleys-waveform allows control of the high-energy electron bombardment at the wafer, which could be used to improve the compensation for positive surface charges inside high-aspect ratio (HAR) etch features.

Figure 9 shows the time-dependent electron flux-energy distribution function at both electrodes for peaks- and valleys-waveforms. The complex power absorption dynamics of dif-

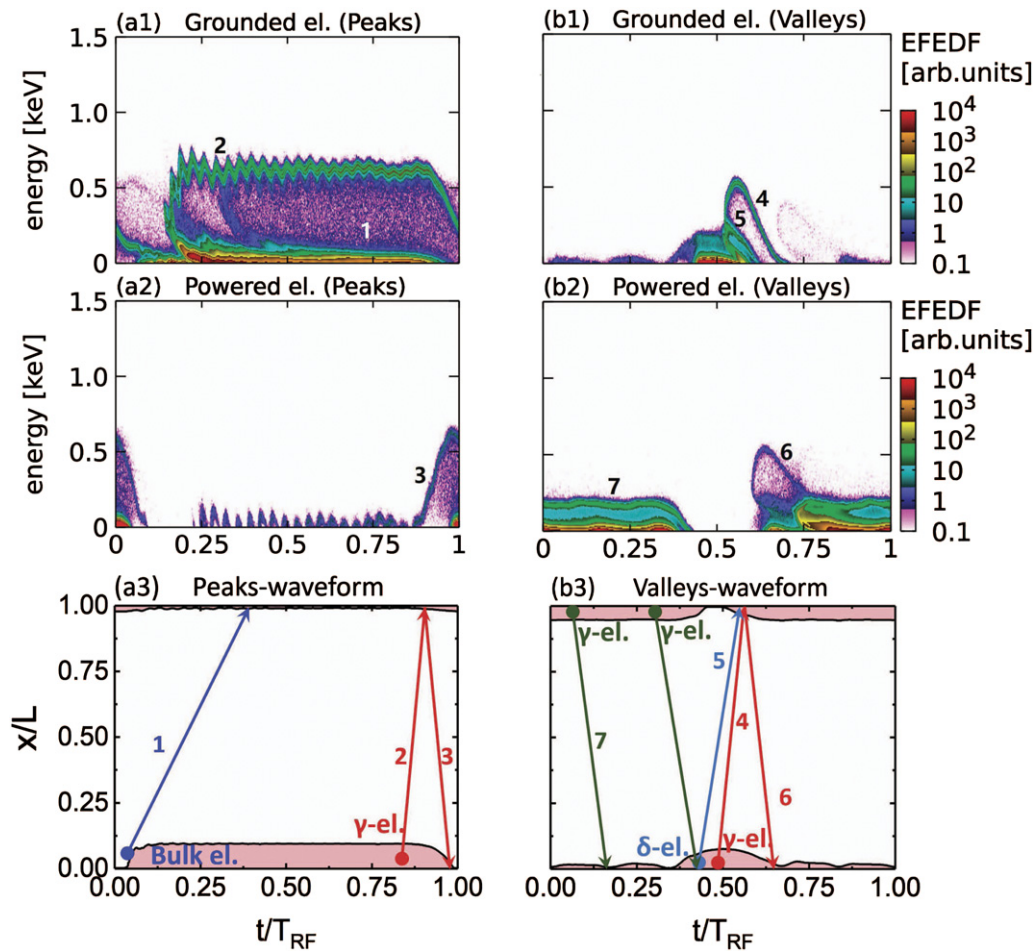


Figure 9. Time-dependent EFEDFs at the planar part of the grounded electrode (first row) and at the powered electrode (second row) for peaks- (first column) and valleys-waveforms (second column). The last row shows schematics of the trajectories of electrons giving rise to the specific features indicated by the numbers in the previous panels. The discharge conditions are the same as in figure 3.

ferent electron groups are found to result in complicated shapes of their distribution functions at the electrodes. In order to understand their formation, the electron flux-energy distribution functions (EFEDFs) obtained in these two cases, where SiO_2 is used as the surface material for both electrodes, were compared to the simulation results where the SEE coefficients at one of the electrodes are set to zero. In this way, the phenomena caused by each specific electron group can be distinguished. A similar analysis method was used by Fu *et al* [112], Vass *et al* [113], and in our own previous work [99]. In the following, we only show the results obtained by including the full SiO_2 surface model in the simulation. Our explanations of the observed features of the time-resolved EFEDFs at the electrodes are, however, based on a detailed analysis of simulation cases where the SEE was switched on and off at the boundary surfaces to identify the electron group causing a given feature.

In the peaks-waveform case, a narrow low-voltage sheath is formed at the grounded electrode. The sheath potential is low during a large portion of the fundamental RF period, which allows a large number of electrons to bombard the electrode.

As shown in figure 9(a1) and marked by ‘1’, a large number of electrons bombards the grounded electrode during $t/T_{\text{RF}} = 0.25\text{--}0.9$ at low energies. At the powered electrode, a large sheath is generated, over which a high potential drops for a large fraction of the fundamental RF period. The γ -electrons emitted at the powered electrode are accelerated towards the bulk in the local sheath, penetrate through the bulk region, and bombard the grounded electrode at high energies during the local sheath collapse. As shown in figure 9(a1), marked by ‘2’ and indicated in figure 9(a3) with the arrow ‘2’, these electrons bombard the grounded electrode at energies up to 700 eV. The oscillations observed in this feature are caused by high-frequency sheath oscillation at the powered electrode, which is induced by the self-excitation of the PSR due to the strong discharge asymmetry. Some of the electrons that bombard the grounded electrode are reflected and return to the powered electrode. If they reach the powered electrode during the local sheath collapse ($t/T_{\text{RF}} = 0.8\text{--}1$ and $t/T_{\text{RF}} = 0\text{--}0.1$), these electrons will arrive with high energies, as shown in figure 9(a2) and marked by ‘3’. For $t/T_{\text{RF}} = 0.1\text{--}0.8$, the sheath potential at the powered electrode is high and only

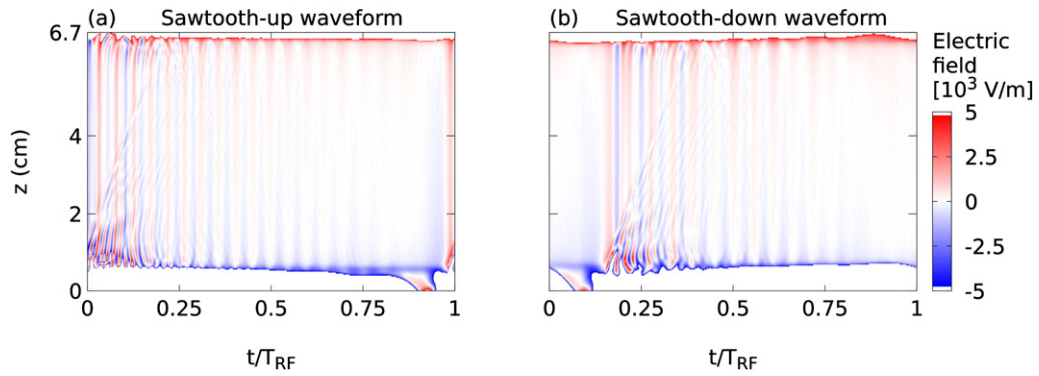


Figure 10. Axially and temporally resolved electric fields for sawtooth-up (a) and sawtooth-down (b) waveforms. The results are obtained by averaging the data in the radial direction within the central region of the reactor ($r \leq 6$ cm). The other discharge conditions are the same as in figure 3.

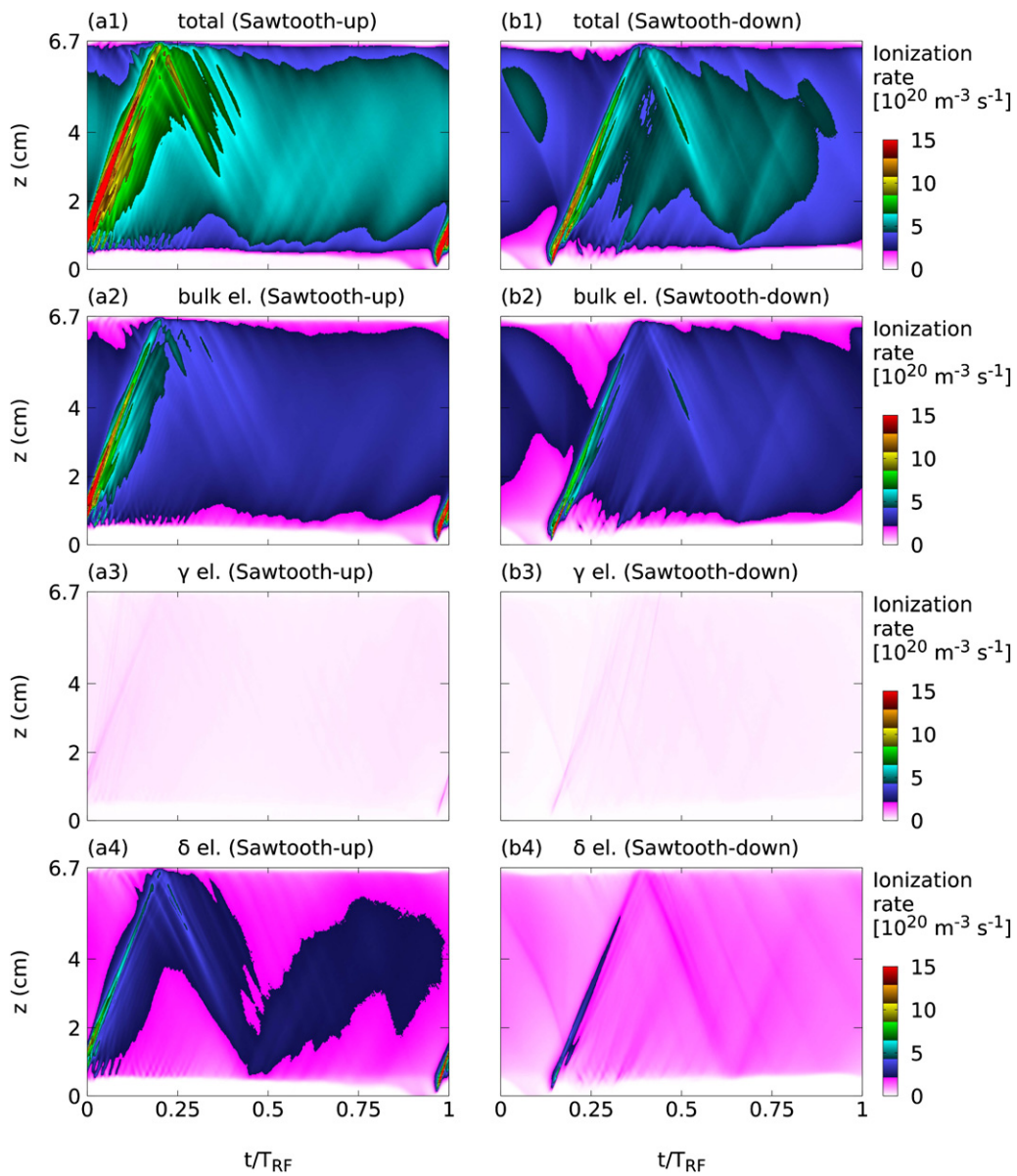


Figure 11. Axially and temporally resolved plots of the total ionization rate (first row), the ionization rate of bulk electrons (second row), γ -electrons (third row), and δ -electrons (fourth row) for sawtooth-up and sawtooth-down waveforms. The results are obtained by averaging the data in the radial direction within the central region of the reactor ($r \leq 6$ cm). The other discharge conditions are the same as in figure 3.

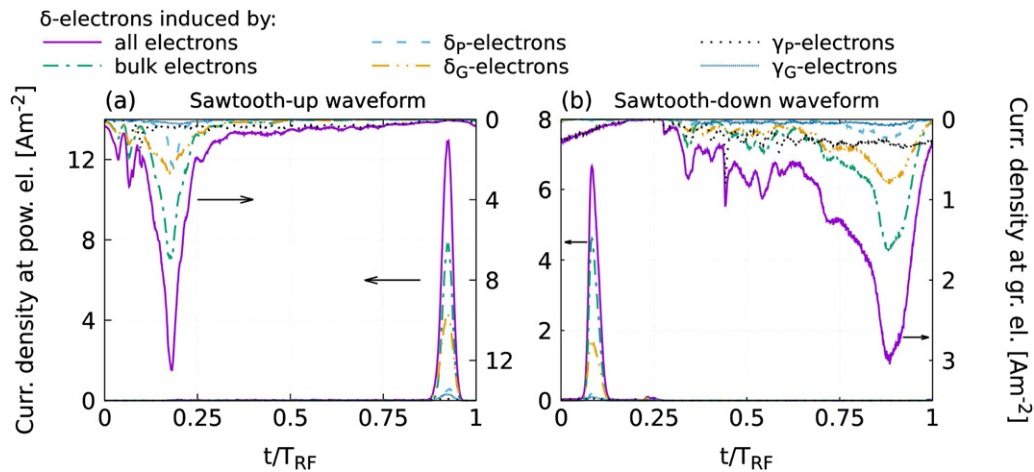


Figure 12. Time-dependent current density of emitted δ -electrons induced by different electron groups at the planar part of the grounded (top and right axes) and the powered (bottom and left axes) electrodes for sawtooth-up and -down waveforms. The other discharge conditions are the same as in figure 3.

high-energy γ -electrons can overcome the sheath potential and bombard the electrode.

In the valleys-waveform case, a large high-voltage sheath is formed at the powered electrode during the time $t/T_{RF} = 0.35-0.65$. The γ -electrons emitted at the powered electrode during this time window are accelerated towards the bulk in the local sheath and reach the grounded electrode at high energies. Thus, in figure 9(b1), an ‘arc’ with a green colour marked by ‘4’ appears, which indicates that these γ -electrons bombard the grounded electrode with energies of up to about 600 eV. Similarly to the peaks-waveform case, after bombarding the grounded electrode, some of these γ -electrons are reflected at the electrode and return to the powered electrode. As shown in figure 9(b2), an ‘arc’ marked by ‘6’ appears during the time $t/T_{RF} = 0.6-0.75$, which indicates this γ -electron bombardment at the powered electrode with energies of up to 600 eV. As the sheath at the grounded electrode is expanded for a large fraction of the fundamental RF period, the γ -electrons emitted at this electrode can be accelerated to high energies during a long time window. If they propagate through the bulk region and arrive at the powered electrode when the local sheath is collapsed, i.e. at $t/T_{RF} = 0-0.35$ and $t/T_{RF} = 0.75-1$, they will bombard this electrode with relatively high energies. If they arrive at the powered electrode when the sheath is partially expanded, they will be able to overcome the local sheath potential and induce δ -electron emission at the electrode surface. Such δ -electrons can be accelerated by the local sheath electric field and bombard the grounded electrode with relatively high energies, as shown in figure 9(b1) with the oblique line marked by ‘5’ and indicated in figure 9(b3) with the arrow ‘5’.

3.3. Detailed analysis of the sawtooth-up and -down waveform cases

The effects of an electrical slope asymmetry on geometrically asymmetric discharges are studied in this section. Axially and temporally resolved electric fields are shown in figure 10 for both types of sawtooth waveform. Due to the geometric reactor

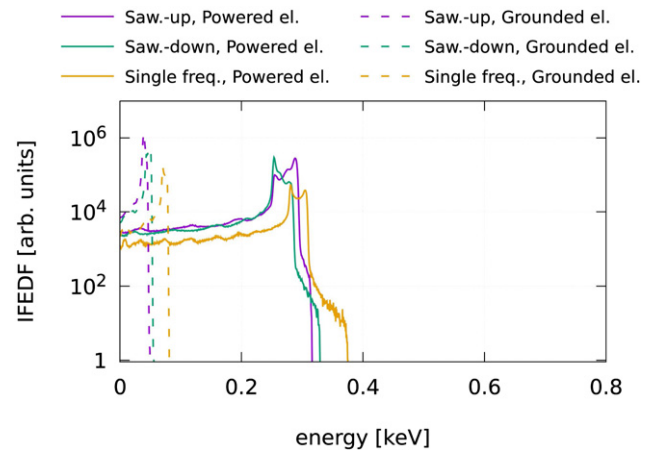


Figure 13. IFEDFs at the powered electrode and at the planar part of the grounded electrode for sawtooth-up and sawtooth-down waveforms, and for the single-frequency case. The other discharge conditions are the same as in figure 3.

asymmetry, the DC self-bias is negative and a large sheath is present at the powered electrode. However, the sheath dynamics are different at both electrodes in the presence of sawtooth waveforms. In the sawtooth-up waveform case, the large sheath at the powered electrode expands fast and collapses slowly. This leads to the excitation of a strong PSR. Compared to this, the sheath expansion at this electrode is slower in the sawtooth-down waveform case. Instead, the sheath at the grounded electrode expands quickly to its maximum width. However, due to the geometric reactor asymmetry, its maximum width is much smaller compared to the sheath width at the powered electrode and, thus, its expansion velocity is lower and a weaker PSR is self-excited. Due to the fast sheath collapse and intensive SEE at the powered electrode, a strong electric-field reversal is generated during the sheath collapse in both cases.

Figure 11 shows the axially and temporally resolved total ionization rate as well as its components caused by different

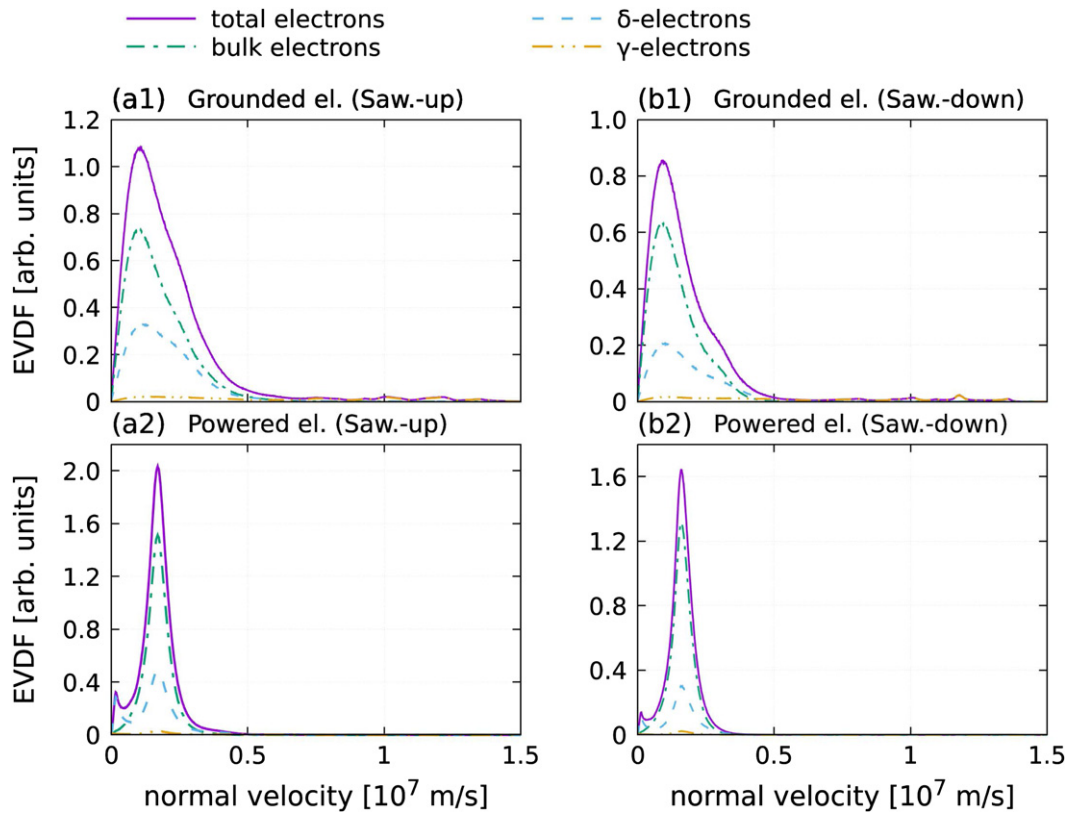


Figure 14. Electron velocity distribution functions at the powered electrode and at the planar part of the grounded electrode for sawtooth-up (first column) and -down waveforms (second column). The other discharge conditions are the same as in figure 3.

electron groups. In the sawtooth-up waveform case, the fast sheath expansion at the powered electrode leads to strong electron power absorption and, therefore, to intensive ionization. This is caused by the constructive superposition of the geometric and electrical slope asymmetries, since the geometric asymmetry causes the sheath voltage and width at the powered electrode to be high via the generation of a negative DC self-bias, and the electrical slope asymmetry causes this sheath to expand to its full width within a short period of time. Energetic electrons generated by sheath expansion heating at the powered electrode propagate through the plasma bulk and bombard the grounded electrode during the local sheath collapse. Some of these electrons, such as the bulk electrons shown in figure 11(a2), are reflected by the electrode and then cause ionization. Moreover, some of these electrons also induce a high number of δ -electron emissions at the grounded electrode. The newly born δ -electrons can cause strong ionization, as shown in figure 11(a4). In this case, the δ -electrons contribute 40% to the total ionization. Other small ionization peaks are observed in figure 11(a1) at times $t/T_{RF} = 0.5$ and $t/T_{RF} = 0.8$, which are caused by the electrons reflected by the sheath near the powered electrode and the electrons accelerated by weak sheath expansion heating at the powered electrode.

In the sawtooth-down waveform case, the sheath at the powered electrode expands more slowly due to the reversed electrical slope asymmetry, i.e., the geometric and electrical slope asymmetries interfere destructively. This leads to weaker

electron power absorption and ionization. The electrons accelerated by this expanding sheath arrive at the grounded electrode, when the local sheath is expanded. Consequently, these electrons have low energy upon their impact at the grounded electrode and release few δ -electrons, which only create weak ionization in the vicinity of this electrode, as shown in figure 11(b4). In this case, the δ -electrons only contribute 30% to the total ionization.

The γ -electrons only induce weak ionization in both cases, since they are too energetic after being accelerated in the sheath—similar to the peaks- and valleys-waveform cases. The reduced plasma density in the sawtooth-down waveform case is mainly due to two reasons: (i) an attenuation of the electron power absorption due to sheath expansion heating at the powered electrode and (ii) an attenuation of δ -electron emission from the electrodes. Similarly to the peaks- and valleys-waveforms, this is ultimately caused by constructive vs destructive superpositions of the geometric and electrical asymmetries. In the case of the sawtooth waveform, the difference in plasma density between the scenarios of constructive and destructive superposition is, however, smaller.

The time-resolved current densities of δ -electrons emitted at both electrodes and their components related to different electron groups are shown in figure 12. The δ -electron current in the sawtooth-up case is found to be much higher than that in the sawtooth-down case at both electrodes. In the sawtooth-up waveform case, a large number of δ -electrons is emitted at the grounded electrode due to bombardment

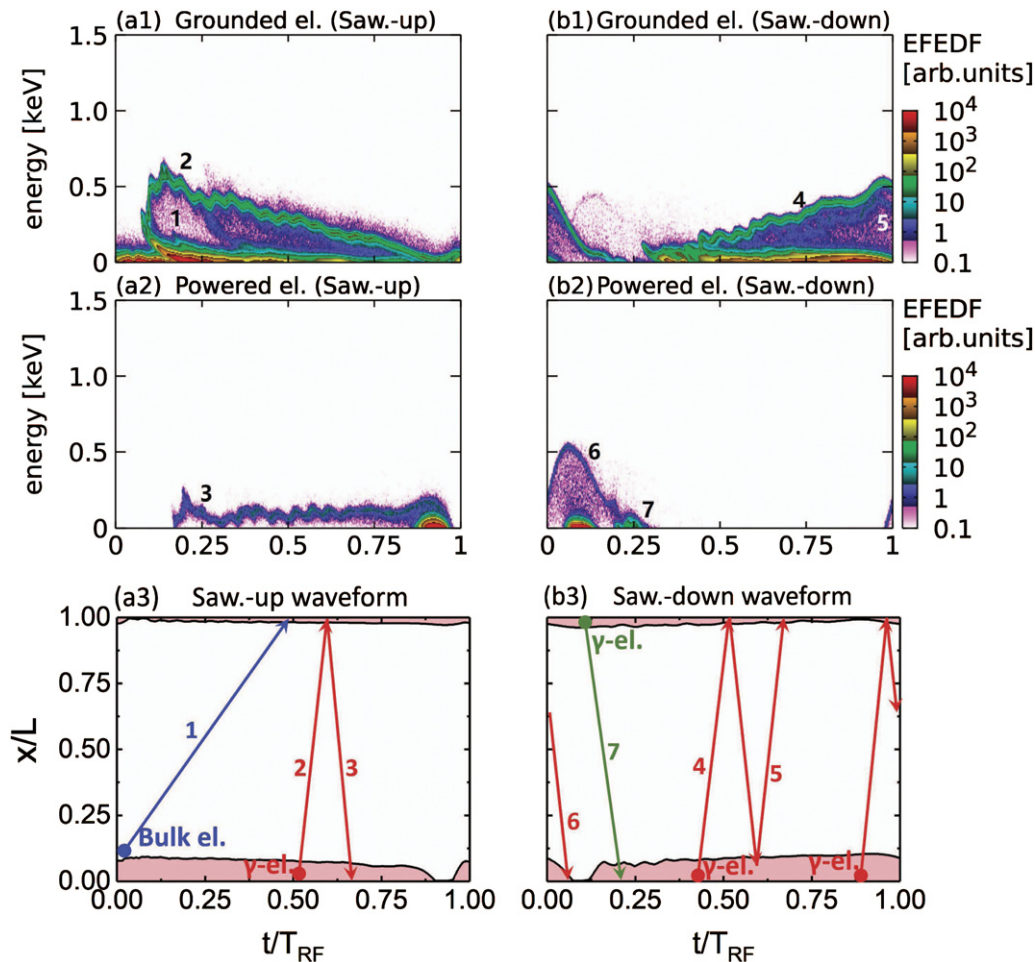


Figure 15. Time-dependent EFEDF at the grounded electrode (first row) and at the powered electrode (second row) for sawtooth-up (first column) and -down (second column) waveforms. The last row shows schematics of the trajectories of electrons that give rise to the specific features indicated by the numbers in the previous panels. The other discharge conditions are the same as in figure 3.

by energetic electrons accelerated by the sheath expansion at the powered electrode. Due to the short sheath expansion phase at the powered electrode and the short total sheath collapse at the grounded electrode, δ -electrons are only emitted within a short time window at the grounded electrode, when the local sheath is collapsed. In the sawtooth-down waveform case, the electrons accelerated by the expanding sheath at the powered electrode bombard the grounded electrode while the local sheath is expanded. Therefore, fewer δ -electrons are emitted in this case. Most of the δ -electrons are emitted during the sheath collapse at both electrodes, when electrons can overcome the local sheath potential and bombard the electrodes.

The IFEDFs for the two sawtooth waveforms and for the single-frequency case are shown in figure 13. In contrast to the peaks- and valleys-waveform cases, the IFEDFs are similar at both electrodes for the sawtooth-up and sawtooth-down waveforms, and for the single-frequency case, due to the similar DC self-bias for these waveforms. The high-voltage sheath at the powered electrode (caused by the negative DC self-bias) leads to large ion-bombardment energies at this electrode. These results show that tuning the waveform from the sawtooth-down to the sawtooth-up type causes an increase of

the plasma density in low-pressure geometrically asymmetric discharges, which enhances the ion flux at the electrodes while keeping the ion bombardment energy almost unchanged.

Figure 14 shows the electron velocity distribution functions at both electrodes for sawtooth-up and -down waveforms. High energy γ -electron bombardment at the grounded electrode is observed in both cases, i.e., several peaks appear at high energies in figures 14(a1) and (b1). These γ -electrons are emitted at the powered electrode and are accelerated in the large high-voltage sheath to high velocities before reaching the grounded electrode. Due to the negative DC self-bias caused by the geometric reactor asymmetry, their energy is high enough to overcome the sheath potential at the grounded electrode. The multiple peaks observed at high electron velocities at the grounded electrode are caused by the several plateaus of the sawtooth driving-voltage waveforms, which lead to an almost unchanged sheath voltage drop during the respective periods of time within each fundamental RF period. The γ -electrons obtain similar energies in the sheath at these respective times. Due to the large high-voltage sheath at the powered electrode, electrons can only reach this electrode during the local sheath collapse. In both cases, a strong electric field reversal is established during sheath collapse, and

electrons are accelerated towards the adjacent electrode by this reversed electric field and bombard the powered electrode at a relatively high energy.

Figure 15 shows the time-resolved electron-flux energy distribution functions at both electrodes. In the sawtooth-up waveform case, the sheath at the powered electrode quickly expands to a large width at the time around $t/T_{RF} = 0(1)$ and gradually collapses (see figure 15(a3)). The fast sheath expansion leads to strong electron power absorption and is ultimately caused by the constructive superposition of the geometric and electrical slope asymmetries for this waveform shape. As a much lower voltage drops across the sheath at the grounded electrode during most of the fundamental RF period, the electrons accelerated near the powered electrode can overcome the sheath potential and bombard the grounded electrode during a long fraction of the fundamental RF period, as shown in figure 15(a1) and marked by '1'. The sheath potential at the powered electrode is relatively high for a long time, when γ -electrons emitted at the powered electrode can be accelerated towards the bulk in the sheath and reach the grounded electrode at high energies. As illustrated in figure 9(a1) by the structure marked by '2' and in figure 15(a3) by the arrow '2', these γ -electrons can bombard the grounded electrode at energies of up to 700 eV. The oscillations shown in figure 9(a1) are caused by the PSR during the sheath expansion at the powered electrode. As the sheath potential at the powered electrode gradually decreases, the γ -electron bombardment energy at the grounded electrode decays as a function of time. Some of these γ -electrons are reflected at the grounded electrode. As the sheath at the powered electrode is collapsing and the instantaneous sheath potential is lower compared to that at the time when the γ -electrons originally left this sheath, these electrons have enough energy to overcome the sheath potential at the powered electrode and reach its surface, as shown in figure 15(a2) with the blue wavy line marked by '3' and in figure 15(a3) with the arrow '3'.

In the sawtooth-down waveform case, a large sheath is generated at the powered electrode due to the geometric reactor asymmetry. This leads to high-energy γ -electron bombardment at the grounded electrode, as shown in figure 15(b1) with the outermost green line marked by '4'. In this case, the sheath voltage at the powered electrode gradually increases during $t/T_{RF} = 0.2-0.9$, which leads to an increasing trend of the line marked by '4'. Similarly to the sawtooth-up case, these γ -electrons can be reflected at the grounded electrode. However, most of the time they cannot reach the powered electrode due to the large local sheath potential. Therefore, these electrons are reflected by the sheath and propagate back towards the grounded electrode again, as shown in figure 15(b1) with the line marked by '5' and in figure 15(b3) with the arrow '5'. Only when the sheath collapses at the powered electrode do γ -electrons reach the powered electrode, leading to the high-energy bombardment of this boundary surface, as shown in figure 15(b2) by the arc '6' and in figure 15(b3) with the arrow '6'. Moreover, a number of electrons is found to bombard the powered electrode at the time $t/T_{RF} = 0.25$. The corresponding feature is marked by '7' in figure 15(b2). These are γ -electrons emitted at the grounded electrode during the local

sheath expansion, where they are accelerated to sufficiently high energies to overcome the sheath potential and arrive at the powered electrode.

4. Conclusions

Using 2D3V electrostatic PIC/MCC simulations, we investigated two different types of the electrical asymmetry effect, i.e. amplitude and slope asymmetries, in geometrically asymmetric capacitive RF discharges operated in argon at low pressure, including realistic SEE processes for SiO₂ surfaces. These electrical asymmetries were induced by peaks-, valleys-, and sawtooth driving voltage waveforms at a fixed peak-to-peak voltage in a reactor that consisted of a large grounded electrode and a small powered electrode. The presence of these electrical asymmetries was found to cause significantly different effects in geometrically asymmetric discharges, compared to those observed previously in geometrically symmetric discharges, as a result of a waveform-dependent constructive or destructive superposition of the geometric and electrical asymmetries.

Compared to single-frequency discharges operated under the same discharge conditions and with identical peak-to-peak driving voltages, the plasma density was enhanced by the use of VWT. However, the effects of the various waveform shapes were found to be different, due to their effects on the plasma symmetry and electron kinetics.

The effects of an electrical amplitude asymmetry were studied by changing the driving voltage waveform from the peaks- to the valleys-type. This was found to lead to strong changes of the sheath and electron power absorption dynamics and finally to a significant reduction of the plasma density. If the discharge was driven by a peaks-waveform, the total plasma asymmetry was enhanced due to a constructive superposition of the electrical amplitude and the geometric reactor asymmetry, which led to the generation of a strongly negative DC self-bias and, thus, to a large high-voltage sheath at the powered electrode. The resulting fast sheath expansion at the powered electrode enhanced the electron power absorption and caused strong ionization. The electrons accelerated by this expanding sheath propagated through the bulk region, bombarded the grounded electrode, and led to intensive δ -electron emission at this electrode. Such δ -electrons led to strong ionization, which finally caused more than half of the total ionization in the discharge. If the discharge was driven by a valleys-waveform, the geometric asymmetry was compensated for by the electrical amplitude asymmetry, i.e. a low positive DC self-bias of 60 V was generated. In this scenario, a narrower and lower-voltage sheath was formed at the powered electrode. The electron power absorption due to the sheath expansion at this electrode was, therefore, attenuated and the ionization rate was reduced. Moreover, the electrons accelerated by the sheath expansion on this side arrived at the grounded electrode when the local sheath was expanded. Therefore, fewer δ -electrons were emitted, and the ionization caused by δ -electrons was reduced. Overall, the attenuated electron power absorption due to sheath expansion heating and the depleted δ -electron emission as a consequence of the destructive

superposition of the electrical amplitude and the geometrical reactor asymmetries were the two main reasons for the reduced plasma density in the valleys-waveform case. Changing the driving voltage waveform also affected the charged particle distribution functions at the electrodes. Switching from the peaks-waveform to the valleys-waveform allowed control of the high-energy γ -electron bombardment at the wafer, which could be used to neutralize positive surface charges at the bottom of HAR etch features.

Slope asymmetry was studied using sawtooth-up and -down waveforms. Due to non-local electron dynamics at low pressure, the different sheath dynamics at both electrodes do not cause significantly different ionization rates at both electrodes over a time average. Consequently, the DC self-bias is almost identical for both sawtooth waveforms. Nevertheless, constructive/destructive superposition of the electrical slope with the geometric reactor asymmetry occurs in the case of sawtooth-up/-down waveforms, respectively. In case of the sawtooth-up waveform, the large high-voltage sheath at the powered electrode expands quickly, generating energetic beam electrons that propagate towards the grounded electrode and cause strong ionization. These energetic electrons reach the opposite electrode at a time of local sheath collapse, so they bombard this boundary surface and cause a strong emission of δ -electrons. Overall, these effects lead to a high plasma density. In the presence of the sawtooth-down waveform, there is destructive superposition of both asymmetries, which attenuates both these effects, resulting in a lower plasma density. Due to the similar DC self-bias for both sawtooth waveforms, the IFEDFs are similar at a given electrode for both waveform shapes. Consequently, switching from a sawtooth-down to a sawtooth-up waveform enhances the ion flux, while the ion and electron energy distributions at the electrodes remain almost unchanged.

In conclusion, the superposition of the electrical amplitude/slope and geometric reactor asymmetries results in different effects of the VWT on the discharge, compared to the previous results obtained for geometrically symmetric plasmas. These different types of asymmetry can interact constructively or destructively, depending on the driving-voltage waveform shape. This interaction strongly affects the plasma density and charged-particle distribution functions at the boundary surfaces. These results are expected to be relevant for applications where most of the capacitively coupled plasma reactors are geometrically asymmetric and where they can serve as a basis for knowledge-based process development and optimization. Clearly, additional investigations into such effects in more complex gas mixtures are required. Moreover, the consequences of these effects on plasma-processing applications such as etching and deposition should be studied.

Acknowledgments

This work was supported by the German Research Foundation within the framework of the project ‘Electron heating in capacitive RF plasmas based on moments of the Boltzmann equation: from fundamental understanding to knowl-

edge based process control’ (No. 428942393); within the framework of the collaborative research centre SFB-TR 87 (Project C1) by the National Office for Research, Development and Innovation of Hungary (NKFIH) via Grant 134462; by the National Natural Science Foundation of China (Grant Nos. 12020101005, 11975067); and by the China Scholarship Council (No. 201906060024).

Data availability statement

The data that support the findings of this study are available upon reasonable request from the authors.

ORCID iDs

Li Wang  <https://orcid.org/0000-0002-3106-2779>
 Peter Hartmann  <https://orcid.org/0000-0003-3572-1310>
 Zoltán Donkó  <https://orcid.org/0000-0003-1369-6150>
 Yuan-Hong Song  <https://orcid.org/0000-0001-5712-9241>
 Julian Schulze  <https://orcid.org/0000-0001-7929-5734>

References

- [1] Lieberman M A and Lichtenberg A J 2005 *Principles of Plasma Discharges and Materials Processing* 2nd edn (New York: Wiley)
- [2] Chabert P and Braithwaite N 2011 *Physics of Radio-Frequency Plasmas* (Cambridge: Cambridge University Press)
- [3] Makabe T and Petrovic Z L 2014 *Plasma Electronics: Applications in Microelectronic Device Fabrication* 2nd edn (Boca Raton, FL: CRC Press)
- [4] Chabert P, Tsankov T V and Czarnetzki U 2021 *Plasma Sources Sci. Technol.* **30** 024001
- [5] Rauf S and Balakrishna A 2017 *J. Vac. Sci. Technol. A* **35** 021308
- [6] Huang S, Huard C, Shim S, Nam S K, Song I-C, Lu S and Kushner M J 2019 *J. Vac. Sci. Technol. A* **37** 031304
- [7] Olevanov M, Proshina O, Rakhimova T and Voloshin D 2008 *Phys. Rev. E* **78** 026404
- [8] Krüger F, Wilczek S, Mussenbrock T and Schulze J 2019 *Plasma Sources Sci. Technol.* **28** 075017
- [9] Donkó Z, Derzsi A, Vass M, Schulze J, Schüengel E and Hamaguchi S 2018 *Plasma Sources Sci. Technol.* **27** 104008
- [10] Bera K, Rauf S, Balakrishna A and Collins K 2010 *IEEE Trans. Plasma Sci.* **38** 3241–8
- [11] Heil B G, Schulze J, Mussenbrock T, Brinkmann R P and Czarnetzki U 2008 *IEEE Trans. Plasma Sci.* **36** 1404–5
- [12] Heil B G, Czarnetzki U, Brinkmann R P and Mussenbrock T 2008 *J. Phys. D: Appl. Phys.* **41** 165202
- [13] Donkó Z, Schulze J, Heil B G and Czarnetzki U 2008 *J. Phys. D: Appl. Phys.* **42** 025205
- [14] Czarnetzki U, Schulze J, Schüengel E and Donkó Z 2011 *Plasma Sources Sci. Technol.* **20** 024010
- [15] Lafleur T 2015 *Plasma Sources Sci. Technol.* **25** 013001
- [16] Bruneau B, Gans T, O’Connell D, Greb A, Johnson E V and Booth J P 2015 *Phys. Rev. Lett.* **114** 125002
- [17] Schulze J, Schüengel E, Donkó Z and Czarnetzki U 2010 *J. Phys. D: Appl. Phys.* **43** 225201
- [18] Bienholz S, Styrnoll T and Awakowicz P 2014 *J. Phys. D: Appl. Phys.* **47** 065201
- [19] Bruneau B et al 2015 *Plasma Sources Sci. Technol.* **25** 01LT02
- [20] Bruneau B et al 2016 *J. Appl. Phys.* **119** 163301

- [21] Derzsi A, Korolov I, Schüngel E, Donkó Z and Schulze J 2013 *Plasma Sources Sci. Technol.* **22** 065009
- [22] Schulze J, Derzsi A and Donkó Z 2011 *Plasma Sources Sci. Technol.* **20** 045008
- [23] Brandt S et al 2016 *Plasma Sources Sci. Technol.* **25** 045015
- [24] Brandt S, Berger B, Donkó Z, Derzsi A, Schüngel E, Koepke M and Schulze J 2019 *Plasma Sources Sci. Technol.* **28** 095021
- [25] Schulze J, Schüngel E, Donkó Z and Czarnetzki U 2010 *Plasma Sources Sci. Technol.* **19** 045028
- [26] Berger B, Brandt S, Franek J, Schüngel E, Koepke M, Mussenbrock T and Schulze J 2015 *J. Appl. Phys.* **118** 223302
- [27] Gibson A R et al 2019 *Plasma Sources Sci. Technol.* **28** 01LT01
- [28] Korolov I, Donkó Z, Hübner G, Bischoff L, Hartmann P, Gans T, Liu Y, Mussenbrock T and Schulze J 2019 *Plasma Sources Sci. Technol.* **28** 094001
- [29] Zhao K, Wen D Q, Liu Y X, Lieberman M A, Economou D J and Wang Y N 2019 *Phys. Rev. Lett.* **122** 185002
- [30] Zhang Y-R, Hu Y-T, Gao F, Song Y-H and Wang Y-N 2018 *Plasma Sources Sci. Technol.* **27** 055003
- [31] Zhang Y, Zafar A, Coumou D J, Shannon S C and Kushner M J 2015 *J. Appl. Phys.* **117** 233302
- [32] Zhang Y-R, Hu Y-T and Wang Y-N 2020 *Plasma Sources Sci. Technol.* **29** 084003
- [33] Zhao K, Su Z-X, Liu J-R, Liu Y-X, Zhang Y-R, Schulze J, Song Y-H and Wang Y-N 2020 *Plasma Sources Sci. Technol.* **29** 124001
- [34] Schüngel E, Mohr S, Schulze J and Czarnetzki U 2015 *Appl. Phys. Lett.* **106** 054108
- [35] Lafleur T and Booth J P 2013 *Appl. Phys. Lett.* **102** 154104
- [36] Korolov I, Donkó Z, Czarnetzki U and Schulze J 2012 *J. Phys. D: Appl. Phys.* **45** 465205
- [37] Bora B, Bhuyan H, Favre M, Wyndham E and Wong C S 2013 *J. Appl. Phys.* **113** 153301
- [38] Schuengel E, Schulze J, Donko Z and U C 2011 *Phys. Plasmas* **18** 013503
- [39] Lafleur T, Delattre P A, Johnson E V and Booth J P 2013 *Plasma Phys. Control. Fusion* **55** 124002
- [40] Johnson E V, Pouliquen S, Delattre P-A and Booth J-P 2012 *Japan J. Appl. Phys.* **51** 08HF01
- [41] Johnson E V, Verbeke T, Vanel J-C and Booth J-P 2010 *J. Phys. D: Appl. Phys.* **43** 412001
- [42] Zhang Y, Kushner M J, Sriraman S, Marakhtanov A, Holland J and Paterson A 2015 *J. Vac. Sci. Technol. A* **33** 031302
- [43] Doyle S J, Gibson A R, Boswell R W, Charles C and Dedrick J P 2020 *Plasma Sources Sci. Technol.* **29** 124002
- [44] Franek J, Brandt S, Berger B, Liese M, Barthel M, Schüngel E and Schulze J 2015 *Rev. Sci. Instrum.* **86** 053504
- [45] Schmidt F, Schulze J, Johnson E, Booth J-P, Keil D, French D M, Trieschmann J and Mussenbrock T 2018 *Plasma Sources Sci. Technol.* **27** 095012
- [46] Wang J, Dine S, Booth J-P and Johnson E V 2019 *J. Vac. Sci. Technol. A* **37** 021303
- [47] Köhler K, Coburn J W, Horne D E, Kay E and Keller J H 1985 *J. Appl. Phys.* **57** 59–66
- [48] Wen D-Q, Kawamura E, Lieberman M A, Lichtenberg A J and Wang Y-N 2017 *J. Phys. D: Appl. Phys.* **50** 495201
- [49] Sansonnens L, Howling A A and Hollenstein C 2006 *Plasma Sources Sci. Technol.* **15** 302–13
- [50] Wen D-Q, Kawamura E, Lieberman M A, Lichtenberg A J and Wang Y-N 2017 *Phys. Plasmas* **24** 083517
- [51] Lieberman M A, Lichtenberg A J, Kawamura E and Chabert P 2016 *Phys. Plasmas* **23** 013501
- [52] Hegemann D, Michlíček M, Blanchard N E, Schütz U, Lohmann D, Vandenbossche M, Zajíčková L and Drábik M 2016 *Plasma Process. Polym.* **13** 279–86
- [53] Hegemann D, Bülbül E, Hanselmann B, Schütz U, Amberg M and Gaiser S 2020 *Plasma Processes Polym.* **18** e2000176
- [54] Schulze J, Schüngel E, Czarnetzki U, Gebhardt M, Brinkmann R P and Mussenbrock T 2011 *Appl. Phys. Lett.* **98** 031501
- [55] Zhang Q-Z, Zhao S-X, Jiang W and Wang Y-N 2012 *J. Phys. D: Appl. Phys.* **45** 305203
- [56] Schüngel E, Eremin D, Schulze J, Mussenbrock T and Czarnetzki U 2012 *J. Appl. Phys.* **112** 053302
- [57] Schulze J, Schüngel E and Czarnetzki U 2009 *J. Phys. D: Appl. Phys.* **42** 092005
- [58] Lafleur T, Schulze J and Donkó Z 2019 *Plasma Sources Sci. Technol.* **28** 040201
- [59] Küllig C, Dittmann K, Wegner T, Sheykin I, Matyash K, Loffhagen D, Schneider R and Meichsner J 2012 *Contrib. Plasma Phys.* **52** 836
- [60] Proto A and Gudmundsson J T 2018 *Plasma Sources Sci. Technol.* **27** 074002
- [61] Liu G-H, Wang X-Y, Liu Y-X, Sun J-Y and Wang Y-N 2018 *Plasma Sources Sci. Technol.* **27** 064004
- [62] Hannesdottir H and Gudmundsson J T 2016 *Plasma Sources Sci. Technol.* **25** 055002
- [63] Proto A and Gudmundsson J T 2018 *Atoms* **6** 65
- [64] Sun G Y, Li H W, Sun A B, Li Y, Song B P, Mu H B, Li X R and Zhang G J 2019 *Plasma Processes Polym.* **16** 1900093
- [65] Wang L, Wen D-Q, Zhang Q-Z, Song Y-H, Zhang Y-R and Wang Y-N 2019 *Plasma Sources Sci. Technol.* **28** 055007
- [66] Gudmundsson J T and Lieberman M A 2015 *Plasma Sources Sci. Technol.* **24** 035016
- [67] Rakhimova T V et al 2006 *IEEE Trans. Plasma Sci.* **34** 867–77
- [68] Rauf S, Bera K and Collins K 2009 *Plasma Sources Sci. Technol.* **19** 015014
- [69] Belenguer P and Boeuf J P 1990 *Phys. Rev. A* **41** 4447–59
- [70] Booth J P, Curley G, Marić D and Chabert P 2009 *Plasma Sources Sci. Technol.* **19** 015005
- [71] Schulze J, Derzsi A, Dittmann K, Hemke T, Meichsner J and Donkó Z 2011 *Phys. Rev. Lett.* **107** 275001
- [72] Schulze J, Donkó Z, Schüngel E and Czarnetzki U 2011 *Plasma Sources Sci. Technol.* **20** 045007
- [73] Donkó Z, Schulze J, Hartmann P, Korolov I, Czarnetzki U and Schüngel E 2010 *Appl. Phys. Lett.* **97** 081501
- [74] Lafleur T, Chabert P and Booth J P 2013 *J. Phys. D: Appl. Phys.* **46** 135201
- [75] Korolov I, Derzsi A, Donkó Z and Schulze J 2013 *Appl. Phys. Lett.* **103** 064102
- [76] Braginsky O, Kovalev A, Lopaev D, Proshina O, Rakhimova T, Vasilieva A, Voloshin D and Zyryanov S 2012 *J. Phys. D: Appl. Phys.* **45** 015201
- [77] Daksha M, Derzsi A, Wilczek S, Trieschmann J, Mussenbrock T, Awakowicz P, Donkó Z and Schulze J 2017 *Plasma Sources Sci. Technol.* **26** 085006
- [78] Daksha M, Derzsi A, Mujahid Z, Schulenberg D, Berger B, Donkó Z and Schulze J 2019 *Plasma Sources Sci. Technol.* **28** 034002
- [79] Derzsi A, Korolov I, Schüngel E, Donkó Z and Schulze J 2015 *Plasma Sources Sci. Technol.* **24** 034002
- [80] Horváth B, Daksha M, Korolov I, Derzsi A and Schulze J 2017 *Plasma Sources Sci. Technol.* **26** 124001
- [81] Horváth B, Schulze J, Donkó Z and Derzsi A 2018 *J. Phys. D: Appl. Phys.* **51** 355204
- [82] Sun J-Y, Wen D-Q, Zhang Q-Z, Liu Y-X and Wang Y-N 2019 *Phys. Plasmas* **26** 063505
- [83] Hartmann P et al 2020 *Plasma Sources Sci. Technol.* **29** 075014
- [84] Derzsi A, Horváth B, Donkó Z and Schulze J 2020 *Plasma Sources Sci. Technol.* **29** 074001
- [85] Ohtsu Y, Matsumoto N, Schulze J and Schuengel E 2016 *Phys. Plasmas* **23** 033510
- [86] Schmidt N, Schulze J, Schüngel E and Czarnetzki U 2013 *J. Phys. D: Appl. Phys.* **46** 505202
- [87] Ries S, Banko L, Hans M, Primetzhofer D, Schneider J M, Ludwig A, Awakowicz P and Schulze J 2019 *Plasma Sources Sci. Technol.* **28** 114001

- [88] Lauro-Taroni L, Turner M M and Braithwaite N S 2004 *J. Phys. D: Appl. Phys.* **37** 2216–22
- [89] Phelps A V, Pitchford L C, Pédoussat C and Donkó Z 1999 *Plasma Sources Sci. Technol.* **8** B1–2
- [90] COP database www.lxcat.net retrieved on January 10 2020
- [91] McEachran R and Stauffer A 2014 *Eur. Phys. J. D* **68** 153
- [92] Hayashi database www.lxcat.net retrieved on January 10 2020
- [93] Hayashi M 2003 Bibliography of electron and photon cross sections with atoms and molecules published in the 20th century - argon *Technical Report NIFS-DATA-072* National Institute for Fusion Science Toki, GIFU, 509–5292 Japan www.nifs.ac.jp/report/NIFS-DATA-072.pdf
- [94] Phelps A V 1991 *J. Phys. Chem. Ref. Data* **20** 557–73
- [95] Phelps A V 1994 *J. Appl. Phys.* **76** 747–53
- [96] Donkó Z 2011 *Plasma Sources Sci. Technol.* **20** 024001
- [97] Donkó Z 1998 *Phys. Rev. E* **57** 7126–37
- [98] Okhrimovskyy A, Bogaerts A and Gijbels R 2002 *Phys. Rev. E* **65** 037402
- [99] Wang L, Hartmann P, Donkó Z, Song Y H and Schulze J 2020 2D Particle-in-Cell simulations of charged particle dynamics in geometrically asymmetric low pressure capacitive RF plasmas *Plasma Sources Sci. Technol.* <https://doi.org/10.1088/1361-6595/abf206> (submitted)
- [100] Phelps A V and Petrovic Z L 1999 *Plasma Sources Sci. Technol.* **8** R21–44
- [101] Sobolewski M 2020 73rd Annual Gaseous Electronics Conf. vol 62 BAPS.2017.GEC.WF2.2 URL <http://meetings.aps.org/link/BAPS.2017.GEC.WF2.2>
- [102] Evans D 1984 *Parallel Comput.* **1** 3–18
- [103] Konstantinidis E and Cotronis Y 2012 Accelerating the red/black SOR method using GPUs with CUDA *Parallel Processing and Applied Mathematics* ed R Wyrzykowski, J Dongarra, K Karczewski and J Waśniewski (Berlin: Springer) pp 589–98
- [104] Derzsi A, Lafleur T, Booth J-P, Korolov I and Donkó Z 2015 *Plasma Sources Sci. Technol.* **25** 015004
- [105] Mussenbrock T, Brinkmann R P, Lieberman M A, Lichtenberg A J and Kawamura E 2008 *Phys. Rev. Lett.* **101** 085004
- [106] Donkó Z, Schulze J, Czarnetzki U and Luggenhölscher D 2009 *Appl. Phys. Lett.* **94** 131501
- [107] Schulze J, Heil B G, Luggenhölscher D, Brinkmann R P and Czarnetzki U 2008 *J. Phys. D: Appl. Phys.* **41** 195212
- [108] Wilczek S, Trieschmann J, Schulze J, Schuengel E, Brinkmann R P, Derzsi A, Korolov I, Donkó Z and Mussenbrock T 2015 *Plasma Sources Sci. Technol.* **24** 024002
- [109] Wen D-Q, Kawamura E, Lieberman M A, Lichtenberg A J and Wang Y-N 2016 *Plasma Sources Sci. Technol.* **26** 015007
- [110] Czarnetzki U, Mussenbrock T and Brinkmann R P 2006 *Phys. Plasmas* **13** 123503
- [111] Wilczek S et al 2016 *Phys. Plasmas* **23** 063514
- [112] Fu Y, Zheng B, Wen D-Q, Zhang P, Fan Q H and Verboncoeur J P 2020 *Plasma Sources Sci. Technol.* **29** 09LT01
- [113] Vass M, Derzsi A, Schulze J and Donko Z 2021 *Plasma Sources Sci. Technol.* **30** 03LT04